Appeared in Optical Manufacturing and Testing IV, H. Philip Stahl, Editor, Proceedings of SPIE Vol. 4451, 432-447, 2001.

Uncertainties in interferometric measurements of radius of curvature

Tony L. Schmitz*, Angela D. Davies**, Chris J. Evans
Manufacturing Metrology Division, National Institute of Standards and Technology

ABSTRACT

The radius of curvature of spherical surfaces may be determined using the well-known radius, or optical, bench. In this method, a figure measuring interferometer is employed to identify the null positions at the best fit spherical surface (cat's eye) and center of curvature (confocal) of the test optic. A linear slide provides motion between these positions and one or more displacement transducers is used to record the displacement between the cat's eye and confocal positions and, hence, the radius of curvature. Measurements of a polished Zerodur sphere have been completed on the X-ray Optics Calibration Interferometer (XCALIBIR) using both Twyman-Green and Fizeau configurations. Mechanical measurements of the spherical artifact have also been completed using a coordinate measuring machine (CMM). Recorded disagreement between the individual transmission sphere measurements and CMM measurements under well-controlled environmental conditions is larger than the limits predicted from a traditional uncertainty analysis based on a geometric measurement model. Additional uncertainty sources for the geometric model, as well as a physical optics model of the propagation of light, are therefore suggested. The expanded uncertainty analysis is described.

Keywords: radius of curvature, interferometry, uncertainty analysis, diffraction

1. INTRODUCTION

The radius of curvature of spherical optical elements is an important physical attribute, especially if accurate results are to be obtained from ray trace models of complex systems. Although the interferometric measurement of radius using a radius, or optical, bench (i.e., a figure measuring interferometer with a linear mechanical axis and position transducer) is a well-known procedure, reported disagreement between industrially available test plates suggests a need for a more detailed understanding of the measurement, as well as a rigorous and defensible generic uncertainty analysis[1]. In this paper, we address these issues. First, a description of radius bench measurements, as well as the procedure implemented at NIST, are provided. Second, measurement results for a nominally 24.466 mm radius, polished Zerodur sphere using both interferometric and mechanical testing are given. The interferometric measurements were performed on the NIST X-ray Optics Calibration Interferometer (XCALIBIR) using f/1.1, f/3.2, and f/4 spherical wavefronts in both the Twyman-Green and Fizeau configurations. The mechanical measurements were performed on the NIST Moore-48 coordinate measuring machine (CMM)[2]. Disagreement between the different f/number measurements on XCALIBIR, as well as the CMM results, establishes the motivation for this investigation. Third, a treatment of both traditional and new sources of uncertainty (based on geometric model of the measurement) that follows the procedures in the ISO "Guide to the Expression of Uncertainty in Measurement (GUM)[3]" and "Guidelines for Evaluating and Expressing the Uncertainty of NIST Measurement Results[4]" is described. Such a thorough treatment of uncertainty is necessary if in-house traceability of radius measurements is desired. Finally, additional uncertainty sources, based on a physical optics model of the measurement, are suggested. Although several other techniques for radius of curvature measurement have been reported in the literature, including templates/test plates, direct image formation/knife-edge test, astigmatism measurement, spherometers, autocollimator with pentaprism, and shearing interferometers[5-6], only the uncertainties associated with radius bench measurements are considered here.

2. MEASUREMENT DESCRIPTION

A radius bench measurement consists of identifying two null positions, confocal and cat's eye, using a figure measuring interferometer (typically a phase measuring interferometer, or PMI) and recording the displacement between the two positions (typically using a displacement measuring interferometer, or DMI, aligned with the part axis to minimize Abbé offset errors)[7]. The confocal position represents the situation when the center of curvature of the reference spherical wavefront coincides with the part's center of curvature. Cat's eye locates the best-fit spherical surface. Twyman-Green and

* tony.schmitz@nist.gov; phone (301) 975-8346; fax (301) 975-4955; National Institute of Standards and Technology, 100 Bureau Drive, MS 8223, Gaithersburg, MD 20899
** Now at the University of North Carolina at Charlotte, Charlotte, NC; ADavies@email.uncc.edu; phone (704) 687-2505.

Fizeau configurations for the radius measurement of a concave spherical surface are shown in Figures 1 and 2, respectively. In each case, either the reference surface or part may be translated during phase shifting.

The setup for radius measurements in the Fizeau configuration on XCALIBIR is shown in Figure 3. In this figure, collimated light is incident on the transmission sphere (TS) from the right, where a spherical wavefront is generated, and continues to the part under test (a black glass sphere is shown). The part is supported on a three-point kinematic mount that is attached to a 300 mm phase shifter, which is supported by the motorized test stand (composed of two angular and three translational, remotely controlled axes). Displacement between the confocal and cat's eye positions is recorded using three DMIs equally spaced around the part's axis. Not shown are the Helium-Neon stabilized laser source (housed in a separate control room and fiber fed to the temperature-controlled laboratory), off-axis parabola used to collimate the light exiting the source single mode fiber, beam splitter, imaging optics, 1024 x 1024 pixel CCD camera, Twyman-Green reference (not used in this setup), and f/4 diverger and 300 mm collimator (used to expand the beam from 50 mm to 300 mm diameter). The source, beam splitter, Twyman-Green reference, imaging optics, and camera reside on an optical bread board that is attached to a 16 ton granite base, which also supports the diverger, collimator, motorized stage, and DMIs (the Twyman-Green reference can also be moved off the bread board directly onto the base to provide equal path measurement conditions). Additionally, the collimator and motorized stage have vacuum-preloaded air bearing mounts to allow manual motions of approximately 3 m along the length of the granite base. The Twyman-Green setup was realized by removing the collimator and TS and using the f/4 aspheric diverger (in conjunction with the Twyman-Green reference flat) directly to locate the two null positions.

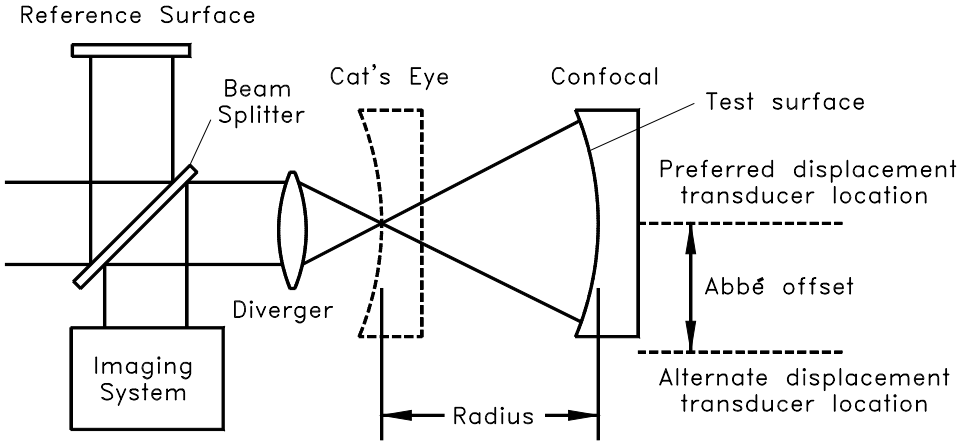

Figure 1: Twyman-Green setup for radius measurement.

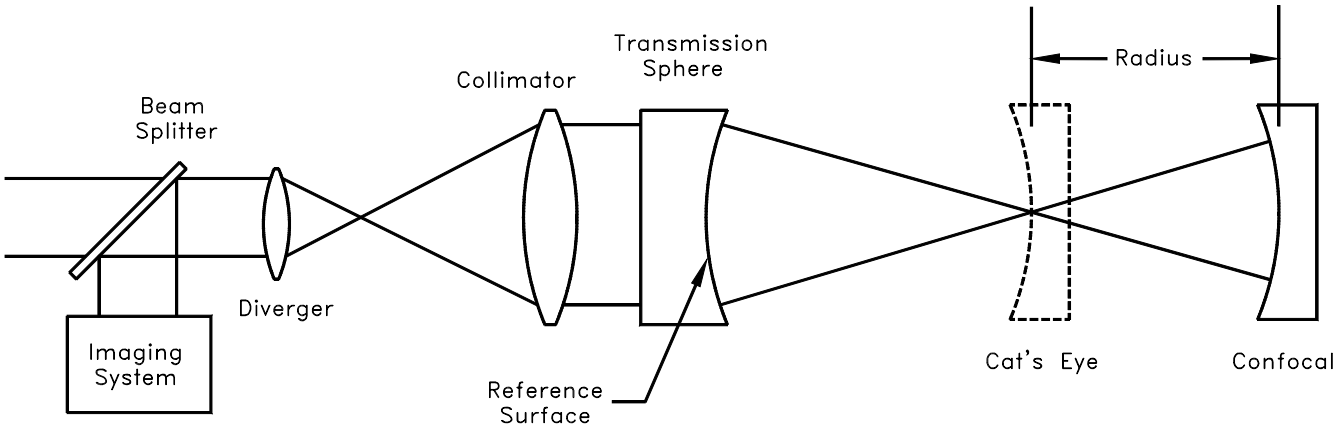

Figure 2: Fizeau configuration for radius measurement.

The series of steps followed to complete a radius measurement for the 24.466 mm Zerodur sphere on XCALIBIR follow. A Twyman-Green configuration measurement using the f/4 diverger is described, but a Fizeau measurement is analogous.

a. Enter XCALIBIR laboratory. Remove the diverger and align the Twyman-Green reference surface using a large retroreflector in the measurement path.

b. Insert shear plate between camera and imaging lens to verify collimation of beam in imaging leg.
c. Insert diverger and align reference surface on diverger mount to Twyman-Green reference.
d. Move ball to confocal position and null fringe pattern using tip/tilt adjustments on motorized test stand.
e. Adjust camera position to obtain best focus on sphere surface. Exit XCALIBIR laboratory.
f. From XCALIBIR control room, define circular software mask to reject any light outside the confocal interferogram.
g. Calibrate piezoelectric transducers (PZTs) used for phase shifting Twyman-Green reference surface.
h. Translate stage along optical axis to cat's eye position to verify that vignetting is not occurring.
i. Return to confocal position and add approximately 3 fringes of power on the opposite side of null from cat's eye.
j. Record the deadpath and unsensed length (these are defined later in the text).
k. Perform ten measurements at small increments along the optical axis toward cat's eye. Adjust the step size to finish at approximately 3 fringes of power on the opposite side of null. At each location, record the displacement using the three DMIs, environmental data (temperature, pressure, and humidity), and Zernike coefficients from the phase measurement.
l. Move to the cat's eye position, again with approximately three fringes of power. Perform ten measurements, recording the same data.
m. Analyze data to determine the two null positions and calculate the radius and associated combined standard uncertainty.

3. EXPERIMENTAL RESULTS

Before proceeding to a treatment of the measurement uncertainty, example results for the experimental radius of curvature of the Zerodur sphere will be provided. Figure 4 shows multiple measurements of the sphere radius over a one month period using: the Fizeau setup displayed in Figure 3 with 150 mm aperture f/1.1 and f/3.2 TSs, the f/4 diverger in the Twyman-Green configuration, and the CMM mechanical measurement (which functions as a cross-comparison). For this data, all known biases from the geometric radius measurement model shown in Figures 1 and 2 have been corrected. The mean and standard deviations of the interferometric measurements are given in Table 1. Please note that the standard deviations do not make any statement about the measurement accuracy, only the spread in the experimental results. Also, the figure does not include error bars defined by the measurement combined standard uncertainty – these will be added in Section 6 after the uncertainty analysis is described. The CMM mechanical comparison result, shown as a dashed line in the figure, is 24.465983 mm with a combined standard uncertainty of 50 nm.

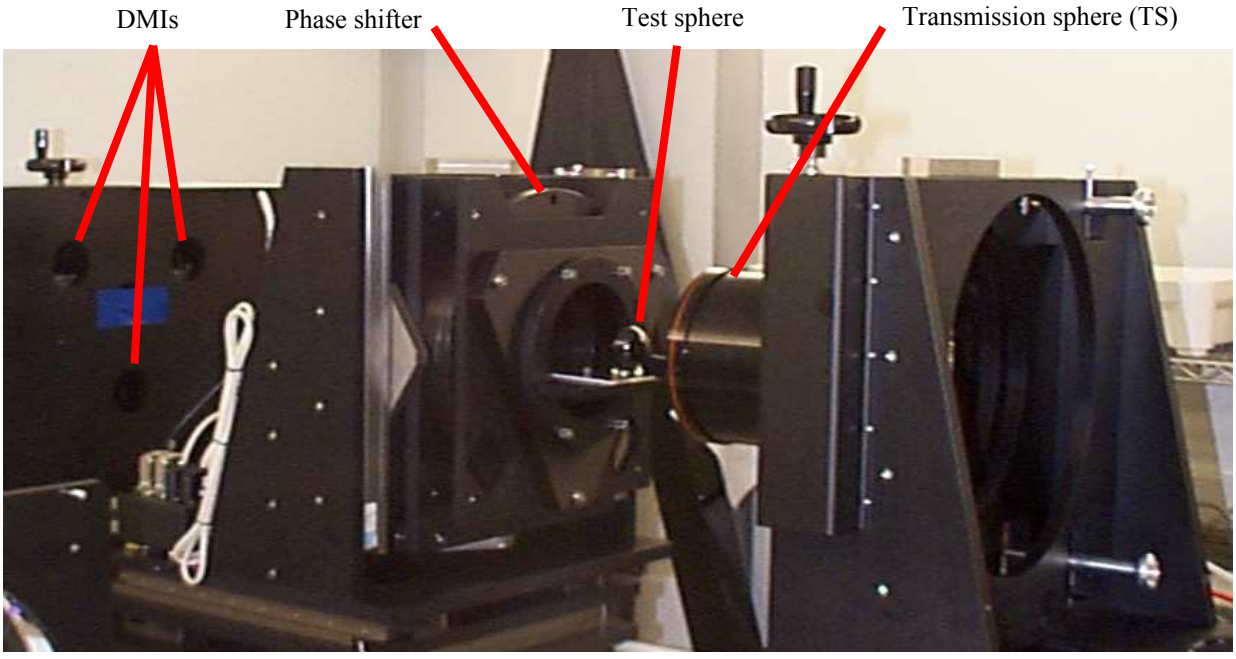

Figure 3: XCALIBIR Fizeau measurement configuration setup.

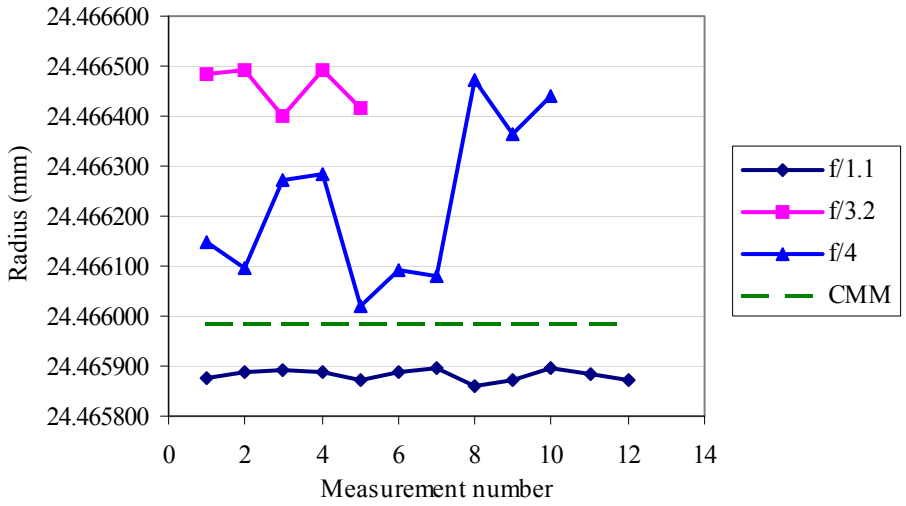

Figure 4: Summary of experimental results for Zerodur sphere.

	Mean radius (mm)	Standard deviation (nm)
f/1.1	24.465878	12
f/3.2	24.466615	45
f/4	24.466540	162

Table 1: Interferometric radius measurement summary.

The data contained in Figure 4 contains artifacts of both repeatability ("closeness of agreement between the results of successive measurements of the same measurand carried out under the same conditions of measurement", Section D.1.1.2[4]) and reproducibility ("closeness of agreement between the results of successive measurements of the same measurand carried out under changed conditions of measurement", Section D.1.1.3[4]). Specifically, the f/1.1 data includes measurements for two independent setups of the TS and motorized test stand; however, the diverger and collimator were not moved (repeatability and partial reproducibility). The f/3.2 measurements were completed on a single setup (repeatability only). The f/4 measurements include four different setups (diverger removed and replaced with subsequent re-alignment of the Twyman-Green reference flat using a large retroreflector). Clearly, an offset is introduced after each new f/4 setup (the measurement sequence was two pairs of trials followed by two trios) which suggests some element of non-reproducibility, most likely due to the alignment sensitivity of the aspheric diverger. Other obvious trends in the data include: 1) biases between the mean values of each of the measurement groups, and 2) degradation in the repeatability of the interferometric data with slower f/number. The disagreement between the different measurement configurations, which is larger than the combined standard uncertainty calculated using a traditional uncertainty analysis and a geometric measurement model (combined standard uncertainty of approximately 26 nm for the radius bench results[8]), requires a closer look at contributors to radius bench measurement uncertainty.

4. GEOMETRIC MODEL UNCERTAINTY ANALYSIS

An uncertainty analysis for interferometric radius of curvature measurements using the geometric model represented in Figures 1 and 2 may be divided into two fundamental categories: 1) mechanical - uncertainty sources concerned with the radius bench (including both the slide and DMIs), and 2) optical - uncertainties associated with the PMI. In the following paragraphs, descriptions of individual error sources, treatment of the associated uncertainties, and example values for measurements on XCALIBIR are provided.

4.1 Mechanical uncertainties

The mechanical uncertainty sources can be subdivided into those that arise from the radius bench slide motions and the displacement measurement using one or more DMIs. The slide motion uncertainties will be treated first, followed by the DMI uncertainty sources.

4.1.1 Slide motion uncertainties

For this category, uncertainties in measured radius occur due to: 1) parasitic or off-axis error motions during the ideally linear slide travel from confocal to cat's eye, 2) misalignment between the interferometric and mechanical axes, and 3) thermal deformations. The first two error sources are analogous to the well-known cosine error and may be treated according to the recommendations in Annex F (F.2.4.4)[3]. These errors cause the measured displacement to be less than the actual motion and results in a single sided distribution of values. The third error source originates from thermal deformation of portions of the mount between the sphere and the DMI measurement path (i.e., the unsensed length). Expansion or contraction of the unsensed length causes a change in the ball position along the part axis, and therefore the confocal and cat's eye positions, without introducing a change in the DMI value(s). Unless otherwise specified, a Type B evaluation ("based on scientific judgement using all the relevant information", Section 4[4]) of these three uncertainty terms will now be presented.

1. Parasitic error motions

The error in radius, e, due to off-axis motions or straightness errors, δ, while moving from confocal to cat's eye can be written as shown in Equation 1, where r is the radius. The variance, equal to the square of the uncertainty, u_1, in the radius is expressed in Equation 2. In this equation, $u^2(\bar{r})$ is the variance in the average of n measurements of r (where $\bar{r}$ is the average value). This variance term is included in the remaining terms in the uncertainty analysis and, therefore, does not need to be treated here. The measurement uncertainty due to straightness errors of motion may then be written as shown in Equation 3, where the uncertainty in γ has been assumed to be equal in magnitude to γ (in rad). If the measured straightness errors of 3 μm in the horizontal (x) direction and 7 μm in the vertical (y) direction of the motorized z-axis slide on XCALIBIR are combined to obtain a resultant maximum straightness of 7.6 μm, the calculated uncertainty for a nominally 24.466 mm sphere is 2 nm.

$$e = r\left(\cos\gamma - 1\right), \qquad \text{where} \quad \gamma = \sin^{-1}\frac{\delta}{r} \tag{1}$$

$$u_1^{\,2} = u^2\left(\bar{r}\right) + \bar{r}^{\,2}u^4\left(\gamma\right) \tag{2}$$

$$u_1 = \bar{r}u^2\left(\gamma\right) = 24.466\times10^6\cdot\left(0.3\times10^{-3}\right)^2 = 2 \text{ nm} \tag{3}$$

Strictly speaking, because $\bar{r}$ is a biased measurement of r due to the asymmetric distribution of experimental values, the reported radius must be corrected. This bias correction is shown in Equation 4. For a nominally 24.466 mm sphere, the positive bias correction is 2 nm.

$$r = \bar{r}\left(1 + u^2\left(\gamma\right)\right) = 24.466\cdot\left(1 + \left(0.3\times10^{-3}\right)^2\right) = 24.466002 \text{ mm} \tag{4}$$

2. Misalignment of interferometric/mechanical axes

Prior to beginning the radius measurements, the motorized test stand z-axis was first aligned to the granite base using a dial indicator. An alignment telescope was then mounted on the test stand and its axis aligned to the granite using a standard line pairs target mounted on the off-axis parabola (recall that this optic collimates the fiber source). Next the optical axis was aligned with the granite base by viewing the fiber source image at the off-axis parabola with the telescope and adjusting the angle of the fiber until the source image was centered in the telescope cross-hairs. The residual uncertainty after this procedure may be treated in the same fashion as parasitic error motions. However, given the small uncertainty in the corrected angular misalignment (estimated at $4\text{x}10^{-5}$ rad), this error may be neglected.

3. Unsensed length

DMIs measure the relative optical displacement between their reference and measurement paths. In XCALIBIR, the reference path is fixed inside the optics housing (which is attached to the granite base), while the measurement path changes with the motion of the moving retroreflector mounted on the test stand. Ideally, the moving retroreflector would be mounted at the test surface so its motion would be directly sensed. In practice, this is not the case and the distance between the moving retroreflector and test surface represents the unsensed length. Unsensed length variations due to thermal deviations during a measurement introduce a radius uncertainty.

A change in length, ΔL, of the unsensed portion of the measurement path can be expressed as shown in Equation 5 and is a function of the thermal expansion coefficient(s) of the material(s) which make up the unsensed length (α), the magnitude of

the unsensed length ($L_{unsensed}$), and variation in temperature, T, from 20 °C (θ). The variance for unsensed length (u_3) is calculated according to the "law of propagation of uncertainty" (Appendix A[4]) and is shown in Equation 6.

$$\Delta L = \alpha L_{unsensed}\theta\,, \qquad \text{where} \quad \theta = T - 20 \ ^\circ\text{C} \tag{5}$$

$$u_3{}^2 = \left(\left(\frac{\partial \Delta L}{\partial \alpha}\right)u(\alpha)\right)^2 + \left(\left(\frac{\partial \Delta L}{\partial L_{unsensed}}\right)u(L_{unsensed})\right)^2 + \left(\left(\frac{\partial \Delta L}{\partial \theta}\right)u(\theta)\right)^2$$

$$= (L_{unsensed}\theta u(\alpha))^2 + (\alpha\theta u(L_{unsensed}))^2 + (\alpha L_{unsensed}u(\theta))^2 \tag{6}$$

Provided the measurement environment is maintained at 20 °C with some associated uncertainty, the first two terms in Equation 6 are zero. XCALIBIR measurements are made in a temperature controlled environment (20 °C) with an expected probability that "almost all" of the temperatures during a measurement lie within ± 0.02 °C due to both temperature transducer uncertainty and thermal gradients. Assuming a normal probability distribution, the uncertainty in temperature is the limit of 0.02 °C divided by 3 (Section 4.6[4]). The 65 mm unsensed length for the measurements shown in Figure 4 is primarily made up of 6061-T6 aluminum with an approximate thermal expansion coefficient of 22.5 μm/m/°C[9]. Equation 7 gives the measurement uncertainty due to unsensed length for the radius measurements on XCALIBIR.

$$u_3 = \alpha L_{unsensed}u(\theta) = 22.5\times 10^3\left(65\times 10^{-3}\right)\frac{0.02}{3} = 10 \text{ nm} \tag{7}$$

4.1.2 DMI uncertainties

The uncertainty in displacement and measured radius using DMIs can be divided into six primary sources: Abbé, cosine, deadpath, environment, turbulence, and laser system. A treatment of these error sources follows.

4. Abbé offset[10]

This error occurs when the measurement axis is not collinear with the axis of the quantity being measured. For example, it exists if the linear displacement transducer on the radius bench is not collinear with the PMI/part axes. Abbé offset can lead to both positive and negative radius errors and is therefore treated differently than errors 1 and 2 in section 4.1.1 of this text. Abbé error, e, is expressed according to Equation 8, where φ is positive or negative change in tip/tilt angle of the part mount relative to the measurement axis normal and A is the offset between the part and measurement axes. The associated variance is given in Equation 9. Because the three DMIs are equally spaced concentrically around the part axis, the average value gives the on-axis equivalent and this error may be neglected for XCALIBIR radius measurements.

$$e = A\cdot\tan\varphi \tag{8}$$

$$u_4{}^2 = \tan^2\varphi\cdot u^2(A) + \frac{A^2}{\cos^4\varphi}u^2(\varphi) \tag{9}$$

5. Cosine

This error is inherent to DMIs. If the laser beam is not exactly parallel with the direction of motion, a proportional difference, i.e., one that increases with the measurement distance is established between the actual path length and the measured length. This length difference is a function of the angle of misalignment, β, and range of travel (the radius, r, in this case) and may be calculated according to Equation 10. The uncertainty is treated as shown for errors 1 and 2 in the previous section and is given in Equation 11. For the 24.466 mm radius sphere with an uncertainty of 0.1 mrad in the alignment between the mechanical and DMI axes, the uncertainty and bias correction are negligible.

$$e = r(\cos\beta - 1) \tag{10}$$

$$u_5 = ru^2(\beta) = 24.466\times 10^6\cdot\left(0.1\times 10^{-3}\right)^2 = 0.2 \text{ nm} \tag{11}$$

6. Deadpath

When the DMI measurement and reference path lengths are not equal at initialization (the zero displacement point), a deadpath displacement error is introduced for any uncompensated change in environmental conditions during the measurement. Since it is impossible to know the exact temperature, pressure, humidity, and air composition at all times, deadpath error is present in all linear displacement interferometers with unequal reference and measurement optical path lengths. The deadpath distance, L_{dead}, is equal to the difference between the reference and measurement optical path lengths at the zero position. Changes in measured displacement due to environmental fluctuations coupled with a nonzero deadpath are expressed according to Equation 12, where Δn and represents a change in the refractive index. Equation 13 expresses the variance in displacement measurement that exists after the deadpath bias correction, shown in Equation 14[11], has been applied.

$$\Delta L = \Delta n L_{dead}\,, \qquad \text{where } \Delta n = n_{current} - n_{initialize} \tag{12}$$

$$u_6{}^2 = \left(\left(\frac{\partial \Delta L}{\partial n}\right)u(n)\right)^2 + \left(\left(\frac{\partial \Delta L}{\partial L_{dead}}\right)u(L_{dead})\right)^2 = (L_{dead}\cdot u(n))^2 + (\Delta n \cdot u(L_{dead}))^2 \tag{13}$$

$$L_{new} = L_{measured} - \Delta L \tag{14}$$

The change in the refractive index of air due to environmental fluctuations may be calculated using a modified version of Edlén's equation[12] (see Equation 15). Using this equation, the nominal index of refraction can be calculated as 1.000271294 under the conditions of standard temperature and pressure (STP): pressure = 760 mm Hg (101323.2 Pa), temperature = 20 °C (68 °F), and relative humidity = 50%. The atmospheric content of carbon dioxide, CO_2, may be taken to be 355 parts per million (ppm). For a change in any one of these values, the refractive index will also change.

$$n = 1 + 271.8\times10^{-6}\,\frac{P}{101325}\,\frac{293.15}{T}\left(1 + 0.54\left(\frac{CO_2 - 300}{1\times10^{6}}\right)\right) - 1\times10^{-8}\,H\,, \tag{15}$$

where P = air pressure (Pa)
T = absolute temperature (°K)
CO_2 = carbon dioxide content (ppm)
H = relative humidity (%)

The variance in the index of refraction of air with pressure, temperature, carbon dioxide content, and relative humidity is written as shown in Equation 16. In this formulation the partial derivatives have been evaluated at STP conditions and the contribution by the uncertainty in air composition has been assumed negligible.

$$u^2(n) = \left(\left(\frac{\partial n}{\partial P}\right)u(P)\right)^2 + \left(\left(\frac{\partial n}{\partial T}\right)u(T)\right)^2 + \left(\left(\frac{\partial n}{\partial CO_2}\right)u(CO_2)\right)^2 + \left(\left(\frac{\partial n}{\partial H}\right)u(H)\right)^2$$

$$= \left(2.6824\times10^{-9}\,u(P)\right)^2 + \left(-9.2719\times10^{-7}\,u(T)\right)^2 + \left(-1\times10^{-8}\,u(H)\right)^2 \tag{16}$$

For the XCALIBIR laboratory environment, transducers are used to measure the temperature, pressure, and humidity in real time to compensate for the atmospheric changes during a measurement. The transducer uncertainty ranges are: 1) ±0.2 hPa (±0.15 mm Hg) for the barometer, 2) ±0.02 °C for the thermistors, and 3) ±2% for the hygrometer (relative humidity sensor). Substitution of these values in Equations 16 and 13 yields the uncertainty due to deadpath error (see Equation 17 where L_{dead} is expressed in m). It should be noted that Equation 17 does not contain the second uncertainty term in the first-order Taylor series approximation listed in Equation 13. This results from environmental correction of the measured displacement which drives the coefficient Δn to zero with some associated uncertainty. Assuming a deadpath of 1.5 m, uniform probability distributions for pressure and humidity, and a normal distribution for controlled temperature, the uncertainty is 50 nm. Note

that this uncertainty scales linearly with deadpath. On XCALIBIR, the maximum deadpath is 3.5 m for the f/4 diverger Twyman-Green measurements, which results in a 118 nm uncertainty.

$$u_6 = L_{dead}\left(\left(2.6824\times10^{-9}\,\frac{0.2\times10^{2}}{\sqrt{3}}\right)^{2}+\left(-9.2712\times10^{-7}\,\frac{0.02}{3}\right)^{2}+\left(-1\times10^{-8}\,\frac{2}{\sqrt{3}}\right)^{2}\right)^{\frac{1}{2}} \tag{17}$$

7. Environment

A change in the index of refraction of air due to environmental fluctuations during a measurement effectively changes the length of the "yardstick" used to find displacement. As the refractive index increases (e.g., due to a decrease in temperature), the wavelength in air decreases and the measured displacement is greater than actual.

The displacement error due to environmental changes is given in Equation 18, where *r* is the radius to be measured. The measurement variance is shown in Equation 19. As with deadpath error, environmental compensation drives the second term in the right half of Equation 19 to zero (i.e., measured displacement is corrected for instantaneous index value). Substitution of the uncertainty in the refractive index of air using the same values as shown in the previous section gives the uncertainty due to environmental fluctuations as a function of measured radius. For a nominal radius of 24.466 mm, the resulting uncertainty is 1 nm. Again, this uncertainty scales linearly with radius.

$$\Delta L = \Delta n \cdot r \tag{18}$$

$$u_7{}^2 = \left(r \cdot u(n)\right)^2 + \left(\Delta n \cdot u(r)\right)^2 \tag{19}$$

8. Turbulence

Optical path difference due to air turbulence in the environment has been investigated empirically by Estler[11] and Bobroff[13]. It was shown that typical airflow velocities in temperature-controlled environments affect the refractive index of air through time-dependent thermal and pressure fluctuations. Specifically, 1) the low thermal diffusivity of air causes thermal inhomogeneities to be mixed before they can come to equilibrium, and 2) turbulent airflow can cause local pressure fluctuations. Experiments were carried out for varying path lengths and air velocities (175 mm to 6 m, and zero to 200 feet per minute, respectively). Reported root mean square (rms) values varied from 1.5 to 10 nm for unenclosed measurements. For our purposes, a normally distributed uncertainty with about a two out of three chance that the measured displacement is bounded by limits of ±6 nm is typical for radius of curvature measurements in the XCALIBIR environment (< 10 linear feet per minute air velocity). See Equation 20 (Type A evaluation, see Section 3[4]).

$$u_8 = \frac{6}{2} = 3 \text{ nm} \tag{20}$$

9. Laser system

The components of the heterodyne laser system that affect the measurement uncertainty are laser wavelength stability, polarization characteristics of the laser beam, interferometer errors from two sources, and electronics linearity. These uncertainty sources are intrinsic to all heterodyne linear displacement interferometers. The manufacturer-specified values associated with the commercial system used in this research are ±10 nm/m, ±0.8 nm, ±0.8 nm, 22 nm/°C, and ±0.8 nm, respectively.

Also considered here is the error that results from imperfect alignment between the optical axes of the polarization-coded two-frequency light and the polarization beam splitter (PBS). If the laser polarization axes are rotated with respect to the PBS axes, frequency mixing results. This causes a periodic or cyclic error in the measurement signal (i.e., the error does not grow infinitely with distance, but oscillates sinusoidally during retroreflector motion). A range of ±2 nm is assumed.

These six uncertainty sources are combined in quadrature according to the "law of propagation of uncertainty" in Equation 21. In this equation, a uniform distribution for each uncertainty source (except temperature which is treated as normally distributed) has been assumed. If a temperature range of 0.02 °C and nominal radius of $24.466\text{x}10^{-3}$ m are inserted, the resulting uncertainty is 1 nm.

$$u_9^2 = \left(\frac{10}{\sqrt{3}}r\right)^2 + \left(\frac{0.8}{\sqrt{3}}\right)^2 + \left(\frac{0.8}{\sqrt{3}}\right)^2 + \left(22\frac{0.02}{3}\right)^2 + \left(\frac{0.8}{\sqrt{3}}\right)^2 + \left(\frac{2}{\sqrt{3}}\right)^2 \text{ nm}^2 \quad (21)$$

The nine mechanical uncertainty terms may now be combined in quadrature to yield the uncertainty for this section of error sources. For a deadpath of 1.5 m, the square root of the sum-of-the-squares (RSS, Section 5.1[4]) combination is 51 nm. The uncertainty is 118 nm for a 3.5 m deadpath. Clearly, the mechanical uncertainty is dominated by the deadpath error on XCALIBIR. A configuration for substantially reducing deadpath is shown in Figure 5.

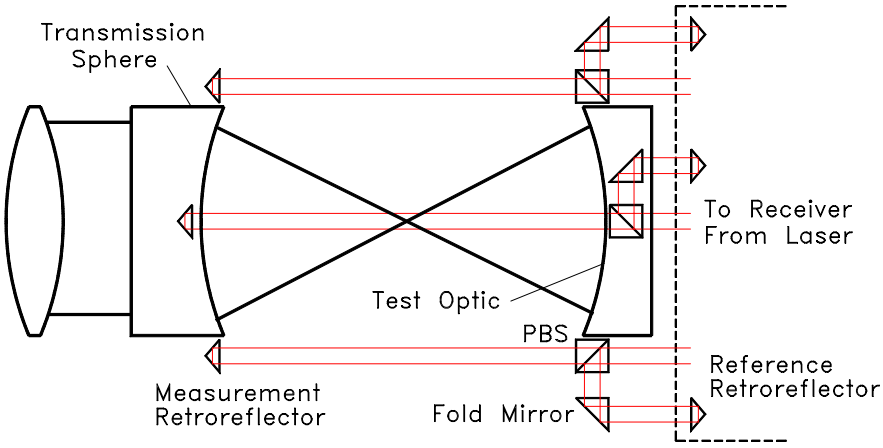

Figure 5: XCALIBIR deadpath reduction scheme (Fizeau configuration in confocal position shown).

4.2 Optical uncertainties

The optical uncertainty sources can be subdivided into three categories: PMI errors, errors introduced by imperfect test surface figure, and radius variation introduced by aperture changes (necessary for comparisons between different f/number measurements) in the presence of figure error. Also included in this section is the uncertainty in locating the confocal and cat's eye null positions using the a_2^0, or power, Zernike coefficient and measured displacement.

10. PMI

Errors in phase measurement affect radius in a number of different ways. First, an uncertainty in the source wavelength has a direct impact since wavelength defines the measured surface height and resulting power. Second, nonlinearities in the phase determination and unwrapping algorithm can lead to power errors. Third, distortion in the imaging optics can corrupt the measured data. In radius measurement, we use the power of a best-fit sphere (to the test optic) to determine the confocal null. After passing through distorted imaging optics, the power term is no longer defined by a fit to the actual surface. Instead, it corresponds to a fit to distorted data and introduces an error. These error sources are highly system specific and should be evaluated for each measurement system independently. For XCALIBIR, they are assumed to be negligible in this analysis, but have not been rigorously explored. A fourth error source is drift in the instrument due to environmental fluctuations during a measurement. This uncertainty component is included in error 13 (Null position location).

A fifth source of uncertainty, treated in the following paragraphs, is the effect of an imperfect spherical wavefront on the measured radius. The conceptual model underlying the use of a radius bench implicitly assumes a perfect wavefront. In laser Fizeau interferometers, the most common PMI configuration for radius bench measurements, all the optics in the source and imaging systems are "common path" and are typically assumed to have negligible effect on the uncertainty of a measurement made near the null condition. Here we use Zemax ray trace code[2] (version 10) to evaluate the uncertainty introduced by that assumption in our radius measurements using an f/1.1 TS.

It is common practice at NIST to evaluate the wavefront of the transmission spheres used in measurements of spherical and aspheric optics. This is accomplished in commercial PMIs (arranged in the Fizeau configuration) by inserting a transmission flat between the instrument and the TS (no test surface beyond the TS is used). This creates a Fizeau cavity between the flat and TS reference surfaces that contains all the elements of the TS. Typical wavefronts for a range of TSs from a variety of manufacturers are shown in Figure 6. Note that all these wavefront departures are an order of magnitude larger than the

departure of the nominally collimated wavefront (evaluated using a shear plate, for example) exiting the commercial Fizeau PMIs used at NIST. In XCALIBIR, the wavefront evaluation is achieved using the Twyman-Green reference flat, rather than inserting a transmission flat in the collimated beam preceding the TS. However, this technique includes the effects of the beam splitter and diverger (which are now located on the measurement cavity).

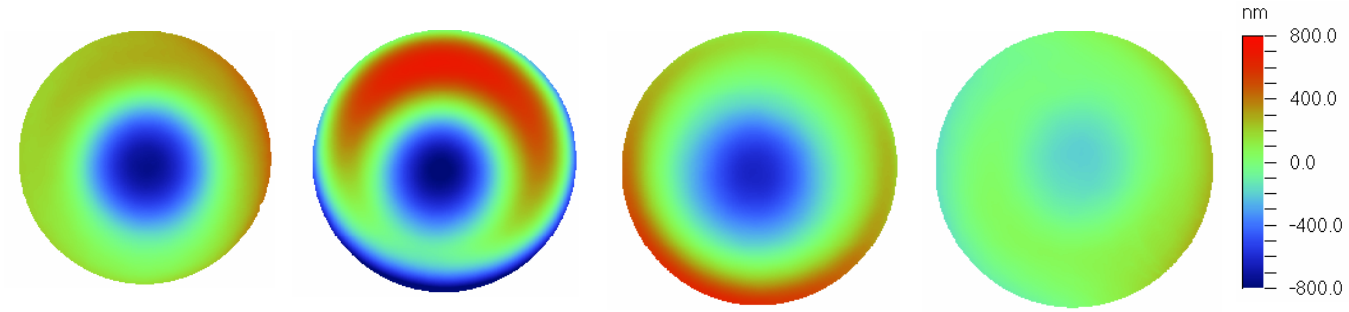

Figure 6: Measured wavefronts of four transmission spheres.

To orient ourselves to the magnitude of possible radius errors due to imperfect wavefront, a simple model was defined using "perfect" thin lens approximations (denoted "paraxial" in Zemax) and a dummy surface used to add aberrations through appropriate Zernike polynomials. The measurement process was simulated by optimizing the position of a 25 mm radius convex test object with respect to the final surface of a 100 mm focal length f/1 "transmission sphere" using the objective function set to give a zero a_2^0 coefficient. Naturally, there were two solutions, confocal and cat's eye, with the distance between them giving radius. Setting the a_4^0 coefficient, or spherical aberration, to 633 nm resulted in a "measured" radius of 25.000045 mm, or a positive bias of 45 nm. On the other hand, adding similar levels of low order rotationally varying terms (e.g., coma and astigmatism) changed the bias at only the nanometer level.

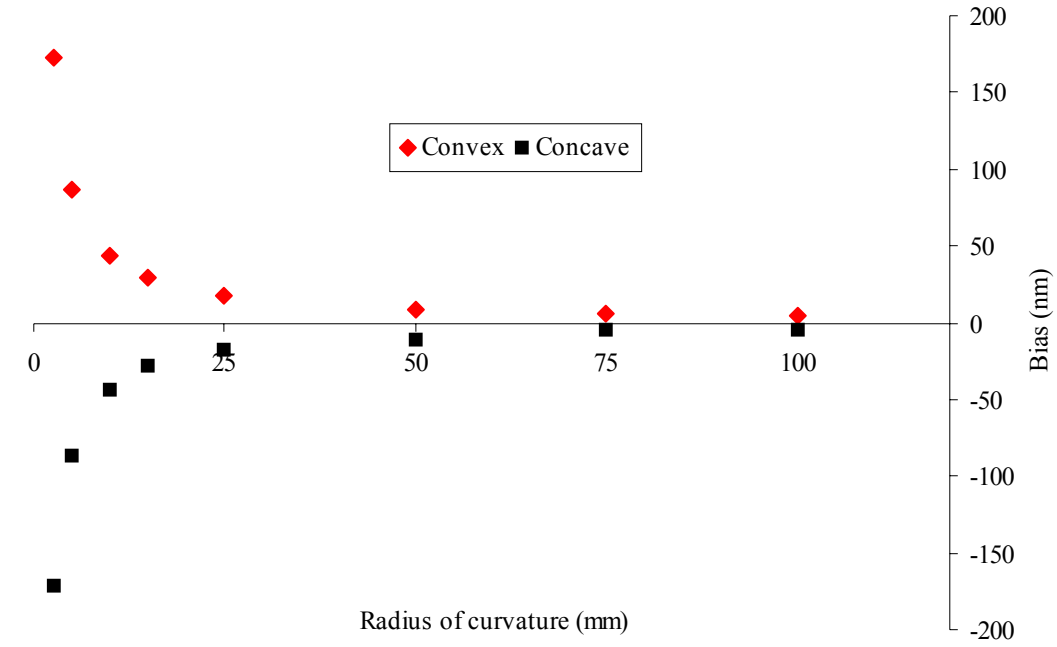

Figure 7: Radius errors due to imperfect wavefront for f/1.1 commercial transmission sphere.

For the actual radius uncertainty evaluation, we use the measured wavefront data and the nominal design of the TS (typically regarded as proprietary information by the manufacturer) in the following manner. The nominal design of the TS is modeled in ray trace code and the measured values of the rotationally invariant Zernike polynomials for the selected TS are used as the objective function for optimization. Our initial experience with the paraxial approximation suggested that the added complexity of treating rotationally varying components was not likely to be worth the effort. All radii of curvature and spacings in the model are set as variables and constrained to tight manufacturing tolerances. Even without allowing for manufacturing imperfections in the surfaces, numerous solutions are possible. Selecting a plausible solution, we then set the

objective function for optimization to be the a_2^0 coefficient of the wavefront (so that the difference in a_2^0 between test and reference beams is zero). As before, we next simulate a radius measurement by optimizing the position of the test object for both the confocal and cat's eye positions. Results of these simulations are shown for a range of radii in Figure 7, where it is seen that the magnitude of the predicted bias increases sharply for small radius values. We choose to treat this radius change as an uncertainty, u_{10}, rather than a correctable bias since there is significant uncertainty in the "reverse engineered" model. Therefore, the uncertainty for the 24.466 mm Zerodur sphere is 18 nm.

11. Surface figure

As noted previously, we define the measurand in a radius of curvature measurement as the radius of a least-squares best-fit sphere over the aperture of the test part. Experimentally this is realized by measuring the displacement between the confocal and cat's eye and positions. At confocal, the power Zernike coefficient is a measure of the best-fit sphere to the test surface and a zero value corresponds to the artifact position where the spherical wavefront exiting the interferometer meets the condition of a best-fit sphere nesting into the test surface. At cat's eye, a zero power term corresponds to the artifact position in space where the cat's eye focus coincides with the center of the artifact surface. If the surface of the test artifact is not perfect, then this surface position at center will be displaced from the best-fit spherical surface. This bias must be removed from the measurement and a residual uncertainty calculated. We call this bias the "figure correction", as demonstrated in Figure 8.

For convenience, consider the figure error of the test artifact in an x-y-z coordinate system on the surface of the best-fit sphere (coordinate system of the phase map of the figure error). The figure error correction, $z(x_0,y_0)$, is determined from a measurement of the figure error, $z_m(x_0,y_0) = z(x_0,y_0) + \varepsilon$, where ε is the measurement noise. We assume the dominant biases have been removed in the measurement of $z(x_0,y_0)$ and, therefore, the expectation of ε is zero.

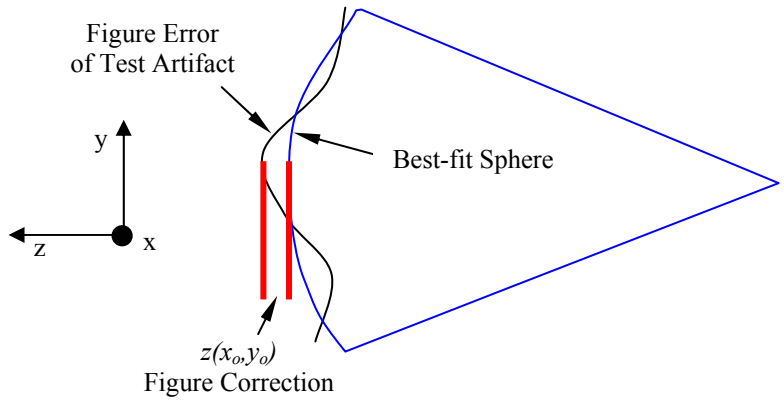

Figure 8: Bias introduced by part figure error.

Two components dominate the uncertainty in the figure correction value, the measurement noise and possible errors in $z(x_0,y_0)$ due to straightness error motions between the confocal and cat's eye positions, which lead to x-y position errors for the cat's eye measurement. The corresponding variance is expressed in Equation 22.

$$u_{11}^2 = \left(\frac{\partial z_m(x_o,y_o)}{\partial x_o} u(\delta_x) \right)^2 + \left(\frac{\partial z_m(x_o,y_o)}{\partial y_o} u(\delta_y) \right)^2 + u^2(\varepsilon) \qquad (22)$$

The first two terms are due to error motions in moving from confocal to the cat's eye position, where the sensitivity coefficients are determined from the slopes of the figure error at the part center in the x and y directions, respectively, and the $u(\delta_{x/y})$ expressions give the straightness uncertainty in the corresponding directions.

The third term is the variance of the noise on a single pixel at or near the center of the phase map. One method of estimating this quantity follows (Type A evaluation):

a) Obtain enough data of the figure error of the test artifact that many estimates of the surface can be generated. The average of all of these estimates will be the final estimate of the figure error. Note that the output of the PMI does not

provide this information; rather, it gives the convolution of the part figure with the interferometer optics contributions. Therefore, a so-called "absolute test" such as the "random ball test"[14] must be performed to isolate the part figure errors.

b) Randomly pair up these single estimates of the part figure error and calculate the difference map of each pair.
c) Define a region at the center of the phase map that approximately corresponds to the area defined by the straightness errors and collect the $z(x,y)$ values in this region. Do this for all of the difference maps.
d) Generate a histogram of these values. The histogram should be centered about zero.
e) The variance of this distribution is two times the variance of the noise on a single estimate (assuming noise is uncorrelated among the single estimates). Divide the distribution variance by two to get the variance on a single estimate.
f) The final estimate of the figure error is the average of all N single estimates. Assuming the noise is uncorrelated among the single estimates, the variance of the noise in the final estimate will be the variance on the single estimates divided by N. This quantity is a good estimate of $u^2(\varepsilon)$.

The figure correction bias and residual uncertainty were determined for the Zerodur sphere using an f/1.1 TS in the Fizeau configuration. A random ball test was completed (using the 25 mm back glass sphere shown in Figure 3) to determine the interferometer wavefront. This result was then subtracted from repeated confocal measurements of the Zerodur sphere to obtain several figure phase maps. The center height pixel of the average of these maps gave a measurement bias of –2 nm. Calculations of the x and y direction slopes for the average map were then combined with the noise and straightness uncertainty to obtain a bias correction uncertainty of 0.2 nm.

12. Aperture variation

In order to compare radius measurements of the Zerodur sphere using multiple f/number spherical wavefronts, the effect of changing the size of the incident cone of light must be considered. Variation in the measurement aperture on the sphere surface (i.e., in the confocal position), when combined with rotationally invariant figure errors (such as spherical aberration), causes a change in the apparent sag and the radius of the best-fit sphere. This leads directly to a radius measurement bias. The procedure for identifying this bias follows:

a) Using the fastest spherical wavefront (f/1.1 in our case), measure the figure error of the test optic (note that the figure must again be isolated from interferometer contributions). This measurement should be performed near the confocal null and the tip/tilt and power contributions removed.
b) Aperture the final result from a) to the desired faster light cone (f/3.2 and f/4 in our case). For the Twyman-Green or Fizeau double pass configurations using a He-Ne source, the sag (nm) of the apertured phase map can be calculated from the Zernike power coefficient (waves) as:

$$sag_{error} = 2 \cdot a_2^0 \cdot 632.8 \tag{23}$$

c) Add the result from Equation 23 to the nominal sag for the radius at that aperture. Use the new sag value , sag_{new}, to calculate the radius, r_{new}, as shown in Equation 24, where a is the aperture. The bias that must be applied to the measurement result is then the difference between value calculated from Equation 24 and the nominal radius.

$$r_{new} = \frac{a^2}{8 \cdot sag_{new}} \tag{24}$$

The required bias corrections when changing from f/1.1 to f/3.2 and f/4 apertures for the Zerodur sphere for measurements on XCALIBIR are summarized in Table 2. The uncertainty in the bias correction can be determined from the estimated error in the Zernike power coefficient. If an error of ± 0.0001 waves in power is assumed, the calculations can be completed again using the stated power variation to arrive at maximum and minimum bias values. These values can then be used to determine the bias correction uncertainty. These uncertainties are given in Table 2 with normal distribution and assumed 2 out of 3 chance that the measured power lies in the specified range (Section 4.5[4]).

f/number	r (mm)	a (mm)	sag_{nom} (mm)	sag_{error} (nm)	r_{new} (mm)	bias (nm)	u_{12} (nm)
f/3.2	24.466	7.645625	0.298657	2.2	24.465838	-162	9
f/4	24.466	6.116500	0.191141	2.1	24.465683	-317	13

Table 2: Summary of aperture bias calculations.

13. Null position location

In general, it is not possible to obtain a perfectly nulled cavity at either the confocal or cat's eye positions. Therefore, a number of phase maps may be obtained and the displacement measured at several small steps through the confocal and cat's eye null positions. A least squares linear best fit to the recorded power coefficient/displacement pairs can then be used to estimate each of the null locations. If the equation of the line is stated in the form given in Equation 25, where c_0 is the intercept, c_1 is the slope, z is the measured displacement, E is the error between the measured and modeled value of the power (this error includes PMI drift due to environmental fluctuations), the standard deviation, S, of the fit is given by Equation 26, where m is the number of measurement points[15].

$$a_{2\,i}^{0} = c_0 + c_1 \cdot z_i + E_i \tag{25}$$

$$S = \sqrt{\frac{\sum_{i=1}^{m} E_i^{\,2}}{m-2}} \tag{26}$$

The null position, z_{null}, for confocal and cat's eye is determined from the corresponding best-fit line slope and intercept according to Equation 27, where the power term in Equation 25 has been set to zero and the error in fit is not considered. The difference between the confocal and cat's eye null positions then defines the artifact radius. The null location uncertainty due to the error in fit is determined according to Equation 28 (Type A evaluation), where the standard deviation in the power fit has been applied. This equation gives two values, a maximum and minimum result for the null location. The maximum and minimum radius values using the two confocal null and two cat's eye null positions (from Equation 28) can then be calculated according to Equation 29.

$$z_{null} = \frac{-c_0}{c_1} \tag{27}$$

$$z_{null,max/min} = \frac{-c_0 \mp S}{c_1} \tag{28}$$

$$r_{max} = z_{confocal,max} - z_{cat,min} \qquad r_{min} = z_{confocal,min} - z_{cat,max} \tag{29}$$

Once the maximum and minimum radius values have been determined, the null location uncertainty can be calculated by dividing the difference between these two values by two to get the one-sided range, then three if a normal distribution that contains nearly 100% of all possible values is assumed. The average calculated uncertainties, u_{13}, for the f/1.1, f/3.2, and f/4 data shown in Figure 4 are 16 nm, 149 nm, and 273 nm, respectively. For this study, 10 points were measured through confocal and cat's eye to determine the null positions; given the resulting uncertainty levels, this is clearly an insufficient number of points for slow systems. The dramatic increase in uncertainty with increasing f/number is due to the decreasing slope of the best-fit line (with displacement plotted on the abscissa and power on the ordinate axis).

5. PHYSICAL OPTICS MODEL CONSIDERATIONS

Thus far, a geometric model of the radius measurement process has been assumed. It is appropriate to ask if a model including a physical optics description of the beam propagation through the system might offer insight into the experimental measurement divergence. Two issues are considered here: Gaussian beam profile and diffraction effects. Other issues not yet evaluated include phase change on reflection (i.e., at confocal all rays are incident on the test surface at ideally normal incidence, while at cat's eye the incident angle varies continuously over the converging beam's aperture) and the Gouy phase anomaly at focus[16].

5.1 Gaussian beam profile

One approach is to consider the interferometer as propagating a Gaussian (laser) beam and assume that the cat's eye reflection takes place at the beam waist. The location of the waist may be displaced from the nominal geometric focus

(assumed for the geometric measurement model), depending on the input beam parameters and the lens system aberrations. A variety of commercial software packages perform Gaussian beam propagation calculations, including Zemax. Specifically, Zemax includes an optimization operand for the distance between a surface and the image space Gaussian waist. Taking the f/1.1 TS as a test case, we set both the wavefront (as described in section 4.2 of this text) and a 200 nm displacement of the Gaussian waist from the geometric focus (approximate level of bias in Table 1) as objectives. Allowing a maximum 6 nm amplitude on the rotationally invariant Zernikes on all the surfaces, the f/1.1 TS model can be reoptimized to place the Gaussian waist on either side of geometric focus. Note, however, that the radius of curvature in the far field can be calculated with respect to the waist. Therefore, displacing the effective position of cat's eye with respect to geometric focus also displaces the position at which a specific radius of curvature is found. Assuming commonly used parameters to describe a Gaussian beam[17], the beam waist radius, w_0, is given by

$$w_0 = \frac{\lambda}{\pi \cdot NA} \tag{30}$$

where λ is the wavelength and NA the numerical aperture. The Rayleigh range, z_R, is expressed as

$$z_R = \frac{\pi \cdot {w_0}^2}{\lambda} = \frac{w_0}{NA} \tag{31}$$

and the phase radius of curvature, $\Re$, by

$$\Re = z + \frac{z_R^2}{z} \tag{32}$$

where z is distance along the optical axis from the beam waist. Clearly the waist and, hence, the Rayleigh range increase for slower optics. For reasonably fast optics and radii greater than a few millimeters, the induced bias is small. In the specific case of the f/4 measurements, the phase radius at 25 mm is offset by 6 nm resulting in a negative bias that must be subtracted from the measurement result. The sag over the beam waist is at the picometer level.

5.2 Diffraction effects

In our measurements of the sphere, the transmission sphere always underfills the part and, therefore, the stop must be an aperture in the interferometer in both the confocal and cat's eye positions. Even when measuring an artifact that is overfilled at confocal, the part cannot be the stop at cat's eye. In both instances, if the interferometer is focussed on the part, the stop cannot be perfectly in focus and, hence, there is some edge diffraction that may result in a bias in the power determination and radius error. Such effects can be addressed by wavefront propagation analyses. Preliminary work is underway at NIST[18].

6. COMBINED STANDARD UNCERTAINTY

All the quantified uncertainty terms and biases, if applicable, can now be combined by the RSS method (we will assume zero covariance) to obtain the combined standard uncertainty, u_c, for radius measurements of the 24.466 mm radius Zerodur sphere on XCALIBIR using the f/1.1, f/3.2, and f/4 spherical wavefronts. The results are shown in Table 3. The combined standard uncertainty values have been applied (in the form of error bars) to the data previously shown in Figure 4. This revision is shown in Figure 9. Note that the expanded uncertainty, U, for these measurements could also be calculated by multiplying the combined standard uncertainty by an appropriate coverage factor, k (a value of 2 defines an interval having a level of confidence of approximately 95% assuming a normal distribution, see Section 6[4]). Many of the uncertainties detailed here are expressed as a function of radius. Therefore, Figure 10 is included to illustrate the varying amplitude of the individual uncertainty terms and combined standard uncertainty for radius values from 2.5 mm to 100 mm. Assumptions for this figure include: 1) convex artifacts measured using an f/1.1 TS Fizeau configuration in the XCALIBIR environment, 2) figure error is identical for each artifact and equal to the Zerodur sphere, 3) nominal deadpath is 1.5 m for the 2.5 mm radius and increases to 1.5975 m for the 100 mm radius, and 4) the standard deviation of the linear regression to identify the null positions does not change with radius and is equal to the Zerodur sphere data. Figure 10 shows that the top three uncertainty contributors are imperfect wavefront, deadpath, and null position location for radii of 50 mm and smaller. For larger radii, unsensed length replaces imperfect wavefront. Note that null position uncertainty increases dramatically for slower systems and a significant number of sample positions through null may become necessary.

Error source	u_i (nm) f/1.1	f/3.2	f/4	Bias (nm) f/1.1	f/3.2	f/4
1. Parasitic motions	2	2	2	2	2	2
2. Axes misalignment	0	0	0	-	-	-
3. Unsensed length	10	10	10	-	-	-
4. Abbé	0	0	0	-	-	-
5. Cosine	0	0	0	0	0	0
6. Deadpath	50	50	118	*	*	*
7. Environment	1	1	1	-	-	-
8. Turbulence	3	3	3	-	-	-
9. Laser system	1	1	1	-	-	-
10. PMI	18	18	18	-	-	-
11. Surface figure	0	0	0	-2	-2	-2
12. Aperture variation	-	9	13	-	-162	-317
13. Null position	16	149	273	-	-	-
14. Gaussian beam	**	**	**	0	-3	-6
u_c (nm)	57	158	298	0	-165	-323

Table 3: Summary of uncertainty terms and biases for 24.466 mm Zerodur sphere measurements. *Terms are dependent on environmental conditions during measurements. **Uncertainty not evaluated.

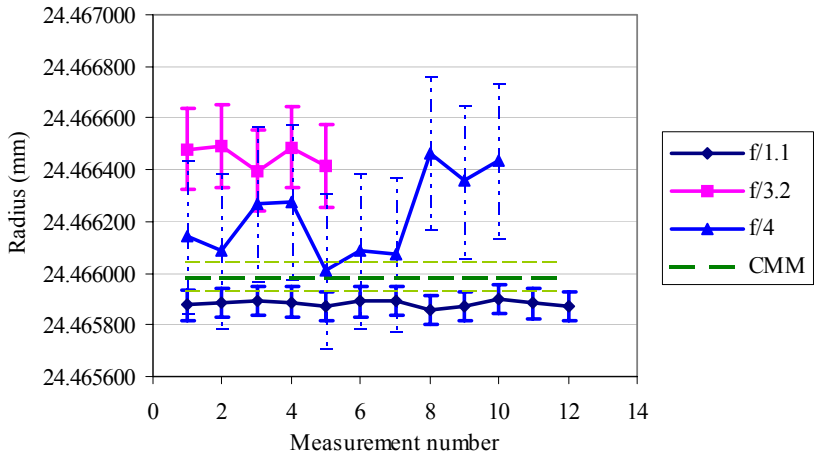

Figure 9: Summary of experimental results for Zerodur sphere with associated combined standard uncertainties.

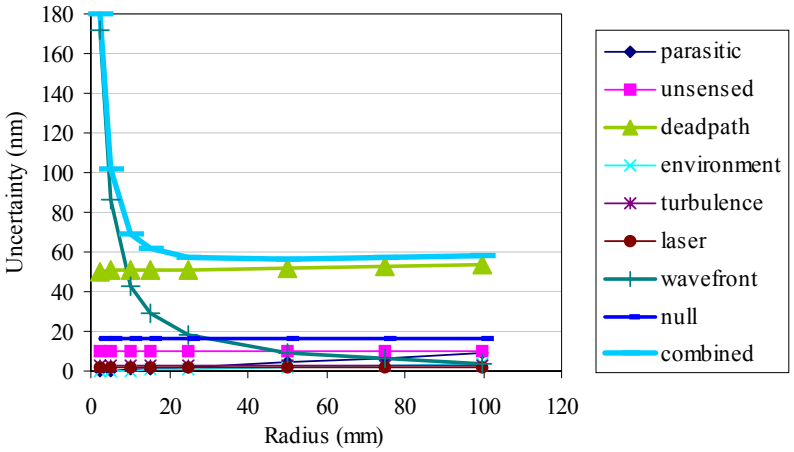

Figure 10: Measurement uncertainty for f/1.1 TS measurements as function of part radius of curvature.

7. CONCLUSIONS

A rigorous uncertainty analysis for interferometric radius of curvature measurements following the procedures in the ISO "Guide to the Expression of Uncertainty in Measurement" (GUM)[3] and NIST Technical Note 1297 "Guidelines for Evaluating and Expressing the Uncertainty of NIST Measurement Results"[4] is presented. An in-depth consideration of error sources affecting radius bench measurements is motivated by significant measurement divergence between mechanical measurements of a polished Zerodur sphere using the NIST M-48 coordinate measuring machine[2] and interferometric measurements on the NIST X-ray Optics Calibration Interferometer (XCALIBIR) in both the Twyman-Green and Fizeau configurations. The uncertainty analysis divides 13 error sources into two separate categories, mechanical and optical, for the typical geometric model of radius measurement and also suggests uncertainty contributors arising from a physical optics description. Primary uncertainty sources include location of the confocal and cat's eye null positions (especially for slow systems), deadpath error in the displacement measuring interferometers used to measure the displacement between the two null positions, and deviations from a perfect spherical wavefront in the phase measuring interferometer (for small radii). Additionally, a significant bias correction that must be applied when comparing measurements of a single artifact with multiple f/number wavefronts is described.

ACKNOWLEDGEMENTS

The authors acknowledge several persons for contributions to this work: R. Kestner of Tinsley Labs, Inc., Richmond, CA and R. Plympton of Optimax Systems, Inc., Ontario, NY helped motivate an investigation into radius measurements; H. Kunzmann, PTB, Braunschweig, Germany, and R. Hocken, Univ. of North Carolina at Charlotte, Charlotte, NC, suggested the consideration of phase at focus and reflection; J. Bruning, Corning-Tropel, Rochester, NY, provided technical suggestions; and T. Doiron and J. Stoup, NIST, completed the mechanical measurements of the Zerodur sphere.

REFERENCES

1. Personal communication with Mr. Rick Plympton, Optimax Systems, Inc., Ontario, NY.
2. Specific commercial equipment is identified to fully describe the experimental procedures. Such identification does not imply any endorsement of the product by the National Institute of Standards and Technology, nor that the product is necessarily the best for the purpose.
3. International Organization for Standardization (ISO), "Guide to the Expression of Uncertainty in Measurement," Geneva, 1995.
4. B. Taylor and C. Kuyatt, NIST Technical Note 1297, "Guidelines for Evaluating and Expressing the Uncertainty of NIST Measurement Results," 1994.
5. D. Malacara, *Optical Shop Testing*, pp. 728-735, John Wiley & Sons, New York, 1992.
6. M. Murty and R. Shukla, "Measurements of long radius of curvature," *Optical Engineering*, **22**, pp. 231-235, 1983.
7. L. Selberg, "Radius measurement by interferometry," *Optical Engineering*, **31**, pp. 1961-1966, 1992.
8. T. Schmitz, C. Evans, and A. Davies, "An investigation of uncertainties limiting radius measurement performance," Proceedings of American Society for Precision Engineering 2000 Spring Topical Meeting – Precision Interferometric Metrology, p. 27, Tucson, AZ, 2000.
9. D. Swyt, "Uncertainties in Dimensional Measurements Made at Nonstandard Temperatures," *Journal of Research of the National Institute of Standards and Technology*, **99**, pp. 31-44, 1994.
10. A. Slocum, *Precision Machine Design*, p. 60, Prentice Hall, Englewood Cliffs, NJ, 1992.
11. W.T. Estler, "High-accuracy displacement interferometry in air," *Applied Optics*, **24**, pp. 808-815, 1985.
12. N. Bobroff, "Recent advances in displacement measuring interferometry," *Measurement Science and Technology*, 4, pp. 907-926, 1993.
13. N. Bobroff, "Residual errors in laser interferometry from air turbulence and nonlinearity," *Applied Optics*, **26**, pp. 2676-2682, 1987.
14. C. Evans, R. Hocken, W.T. Estler, "Self-calibration: reversal, redundancy, error separation, and 'absolute testing'," *Annals of the CIRP*, **45**, pp. 617-634, 1996.
15. S. Chapra and R. Canale, *Numerical Methods for Engineers*, p. 291, McGraw-Hill Book Co., New York, 1985.
16. R. Boyd, "Intuitive explanation of the phase anomaly of focused light beams," *Journal of the Optical Society of America*, **70**, pp. 877-880, 1980.
17. P.C.D Hobbs, *Building Electro-optical Systems*, p. 12, John Wiley & Sons, New York, 2000.
18. E. Shirley, Optical Technology Division, National Institute of Standards and Technology.